Nucleation, surface growth and coagulation of soot by hierarchical modeling

Fakharnezhad, A.; Kelesidis, G. A.; Berry, J. D.; Goudeli, E.

DOI
10.1016/j.powtec.2025.121747

Publication date
2026

Document Version
Final published version

Published in
Powder Technology

Citation (APA)
Fakharnezhad, A., Kelesidis, G. A., Berry, J. D., & Goudeli, E. (2026). Nucleation, surface growth and coagulation of soot by hierarchical modeling. *Powder Technology*, *469*, Article 121747. https://doi.org/10.1016/j.powtec.2025.121747

Powder Technology 469 (2026) 121747

Contents lists available at ScienceDirect

Powder Technology

journal homepage: www.journals.elsevier.com/powder-technology

Nucleation, surface growth and coagulation of soot by hierarchical modeling☆

A. Fakharnezhad [a], G.A. Kelesidis [b], J.D. Berry [a], E. Goudeli [a,*]

[a] Department of Chemical Engineering, The University of Melbourne, Parkville, Melbourne, VIC, Australia
[b] Faculty of Aerospace Engineering, Delft University of Technology, Kluyverweg 1, 2629 HS Delft, the Netherlands

HIGHLIGHTS

- MD suggests a power law dependence of the nucleation rate on fuel concentration.
- A MD-informed particle dynamics model captures the measured soot volume fraction.
- The MD-based model outperforms semi-empirical nucleation rates.

GRAPHICAL ABSTRACT

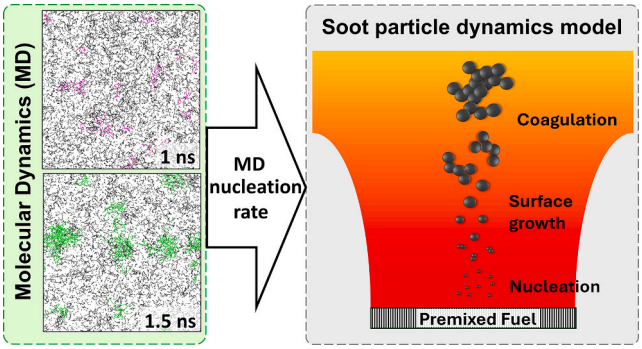

ARTICLE INFO

Keywords:
Soot
Nucleation rate
Reactive molecular dynamics
Monodisperse particle dynamics

ABSTRACT

A hierarchical modeling approach is presented for describing soot growth dynamics, encompassing reactive Molecular Dynamics (MD) simulations and a monodisperse particle dynamics model. Reactive MD is employed to investigate nucleation of soot nanoparticles during isothermal acetylene pyrolysis at 1200–1800 K. A "lumped" soot nucleation rate is determined by tracking the rate of formation of soot clusters at various fuel concentrations, following a power law dependency with the initial acetylene concentration. The MD-obtained soot nucleation rate is incorporated in a monodisperse particle dynamics model describing soot formation in laminar premixed methane flames. The soot volume fraction predicted by the monodisperse model with the MD-derived nucleation rate is in good agreement with measurements in a methane nucleation flame (φ = 1.95), showing significant improvement (3 orders of magnitude) compared to a semi-empirical nucleation rate. The MD-derived nucleation rate also performs well in the methane sooting flame (φ = 2.32), yielding soot volume fractions comparable to experimental measurements.

☆ This article is part of a Special issue entitled: 'Pratsinis' published in Powder Technology.

* Corresponding author.
E-mail address: eirini.goudeli@unimelb.edu.au (E. Goudeli).

https://doi.org/10.1016/j.powtec.2025.121747
Received 1 May 2025; Received in revised form 22 September 2025; Accepted 9 October 2025
Available online 10 October 2025

1. Introduction

Reducing soot emissions is critical in hard-to-abate sectors, such as aviation, heavy-duty transportation, and steel manufacturing, which continue to rely on fossil fuels [1]. Developing cleaner combustion devices is essential for eliminating soot emissions but requires better understanding of soot growth dynamics [2]. Soot formation begins with combustion of hydrocarbon fuels, which decompose into small radicals that initiate reactions producing large polycyclic aromatic hydrocarbons (PAHs) [3]. These PAH precursors nucleate to form incipient soot particles that grow via surface reactions and coagulation into agglomerates, while further downstream in the process, oxidation of soot with O_2 and OH reduces the particle mass and diameter [4].

Soot dynamics have been traditionally simulated by macroscopic models, including method of moments [5,6], kinetic models [7], and population balance equations (PBE) [8,9] coupled with computational fluid dynamics [10,11]. Such models determine the evolution of the soot number density, $\overline{N}$, and volume fraction, f_v, while accounting for the agglomerate structure using empirical correlations based on the fractal dimension [7,12]. Mesoscale models, such as discrete element method (DEM) [13] or Monte Carlo simulations [14,15] describe the detailed dynamics of soot morphology during surface growth and coagulation in flame reactors. That way, easy-to-use relations for the soot agglomerate structure [16] and polydispersity [17] have been derived and interfaced with PBEs to improve the accuracy of the estimated soot $\overline{N}$ and f_v [18]. Still, such DEM [13] and PBE simulations [18] rely on the measured soot nuclei to close the soot mass balance, as there is a large uncertainty associated with the particle nucleation mechanism and rate.

The existing mechanisms of soot nucleation can be classified into three main categories: chemical, physical, and hybrid nucleation [19]. Chemical nucleation involves gas-phase reactions of acetylene (C_2H_2-based) and between PAH radicals (PAH-based) that lead to solid soot nanoparticles [19]. This mechanism faces thermodynamic and kinetic limitations at flame temperatures as hydrogen abstraction and covalent bond formation [20], or formation of reactive sites on PAH surfaces, are only favorable at high temperatures and cannot explain the rapid soot formation observed experimentally in flames [19]. Physical nucleation occurs when PAHs dimerize through physical forces (e.g., van der Waals) to form soot nuclei. However, physical dimerization of moderate sized PAHs, such as pyrene, can be reversible at high temperature flame conditions, making dimers unstable [20,21]. Larger PAHs may provide stronger interactions [20], but their decreasing concentration with increasing PAH size limits their role in nucleation [22]. Hybrid mechanisms that combine physical and chemical nucleation have been proposed, suggesting enhanced dimer stability through chemical bond formation [19]. Despite some calculated kinetic constants [23], these mechanisms require further integration into detailed models and validation against experimental data. Recent findings show that reactive dimerization of PAHs can limit nucleation reversibility, emphasizing the need to incorporate both mechanisms in soot formation models [24,25].

Detailed soot models account for nucleation by solving rate equations of elementary gas-phase reactions up to the formation of PAHs (the most commonly considered soot precursors [26]), and dimerization reactions of those PAHs. One of the most recognized detailed model is the comprehensive framework by Frenklach et al. [27], which outlines detailed reaction pathways for PAH formation and subsequent soot nucleation. While these models offer greater generalizability compared to C_2H_2-based soot nucleation models and can be applied across a wide range of conditions, they often rely on gas-phase reaction mechanisms for predicting PAH formation, which require reaction rate constants for individual reactions [28]. The inclusion of many species and reactions in these gas-phase mechanisms is computationally demanding, making them impractical for real-world applications. Even though simpler C_2H_2-based nucleation rates have been proposed, such as the Lindstedt [29] and Moss-Brookes nucleation rates [30], they are semi-empirical in nature and have been developed for a limited range of conditions. Furthermore, one of the largest uncertainties in the soot nucleation mechanism from PAHs lies in predicting the transition from gas molecules to solid particles. Despite ongoing research, the precise mechanism of soot nucleation remains elusive due to the complexity of the chemical reaction network and due to the difficulty of directly observing nucleation dynamics in experiments, which occur rapidly (within microseconds [31]) and at high flame velocities.

Despite advancements in understanding soot nucleation mechanisms, there is still no consensus on which specific PAHs contribute to soot formation and the mechanisms behind this transition. Ab initio approaches can provide insight into soot formation pathways [32] without knowing or assuming the contributing precursor molecules. For example, reactive molecular dynamics (MD) simulations [33] have been used to propose an "ab initio" expression for the nucleation rate of soot nanoparticles formed during *n*-heptane pyrolysis at high temperature by tracking the formation of clusters.

Here, reactive MD is employed to investigate soot nucleation during acetylene pyrolysis in a typical flame temperature range (1200–1800 K) and different acetylene concentrations. The soot nucleation rate is determined by MD without prior assumptions about the chemical reaction network or nucleation mechanisms. An easy-to-use "lumped" nucleation rate equation is proposed as a function of concentration of acetylene, a key intermediate formed during combustion of many hydrocarbon fuels that drives PAH and soot formation [27] and serves as an indicator of the soot nucleation zone in flames [29]. The MD-obtained soot nucleation rate is interfaced with CHEMKIN PRO [34] and a monodisperse particle dynamics model, and is benchmarked against soot volume fraction measurements in low-pressure premixed methane flames [35] and semi-empirical correlations [30].

2. Theory

2.1. Reactive molecular dynamics (MD) simulations

Isothermal reactive MD simulations of acetylene pyrolysis were performed at 1200–1800 K, corresponding to the typical temperature range for soot formation in methane [36] and ethylene [37,38] premixed flames. A total of 10,000 acetylene molecules were distributed randomly in a cubic simulation cell, with initial fuel density ranging from 0.05 to 0.1 g/cm^3 (corresponding to 1.92–3.84 kmol/m^3), using MAPS Scienomics 4.4 [39]. All MD simulations were performed with periodic boundary conditions in the NVT (constant number, volume, temperature) ensemble, using ReaxFF forcefield for hydrocarbons [40] in LAMMPS [41] with integration time step of 0.25 fs [42].

2.2. Nucleation rate by reactive MD

The nucleation rate, J, is calculated by tracking the rate of change in the number density, $\overline{N}_{n\geq\overline{n}}$ ($\frac{\#}{m^3}$), of clusters with size larger than a threshold size, $\overline{n}$ [43]:

$$J = \frac{d\overline{N}_{n\geq\overline{n}}}{d\,t} \tag{1}$$

where t is the elapsed time. Eq. 1 is applied in the nucleation-dominant region, where the rate of cluster formation is constant [43]. This region corresponds to the time frame where the number of clusters increases linearly with time. When $\overline{n}$ exceeds the critical cluster size, steady-state nucleation is reached and the rate of change of the cluster concentration becomes independent of the cluster size [43,44].

2.3. Gas-phase kinetics by CHEMKIN PRO

Two low-pressure premixed methane flames by Desgroux et al. [35] are simulated using the PREMIX code in CHEMKIN PRO [34] with the

CaltechMech reaction mechanism [28]. The inlet fuel compositions correspond to equivalent ratios, φ, of 1.95 (nucleation flame) and 2.32 (sooting flame) [35: Table 1]. A total flow rate of 3.96 L/min STP and pressure of 26.7 kPa were used for both flames. A fixed gas temperature profile, obtained from experimental measurements [36], was applied in each flame. The convergence criterion is defined with an absolute tolerance of 10^{-9} [45] in the species mass fractions. Temperature-gradient-induced mass diffusion is considered, and mixture-averaged diffusion coefficients are applied.

2.4. Soot dynamics

A monodisperse particle dynamics (PD) model [46] is used to describe soot dynamics during concurrent nucleation, surface growth, and coagulation by tracking the total aggregate number, N, surface area, A, and carbon molar concentrations, C. The nucleation rate obtained by MD and the temperature and acetylene profiles obtained by CHEMKIN PRO are used as input in the PD model (workflow in Fig. S1). The rate of change of the total aggregate number concentration, $\frac{dN}{dt}$, increases due to particle formation by nucleation and decreases due to particle consumption by coagulation:

$$\frac{dN}{dt} = \left(\frac{dN}{dt}\right)^{Nucl.} + \left(\frac{dN}{dt}\right)^{Coag.} \tag{2}$$

Similarly, the rate of change in total carbon molar concentration, $\frac{dC}{dt}$, increases by nucleation and surface growth:

$$\frac{dC}{dt} = \left(\frac{dC}{dt}\right)^{Nucl.} + \left(\frac{dC}{dt}\right)^{SG} \tag{3}$$

The evolution of the total aggregate surface area concentration, A, is [47]:

$$\frac{A}{N}\Big/\frac{a_0}{v_0} = \left(\frac{V}{N}\Big/v_0\right) D_s/3 \tag{4}$$

where a_0 and v_0 denote the primary particle surface area and volume, respectively, V is total aggregate volume concentration ($V = \frac{C\,MW_c}{\rho_{soot}}$), and D_s is the surface fractal dimension quantifying the morphology of soot aggregate, with $D_s = 2$ corresponding to smooth spherical particles and $D_s = 3$ to agglomerates with primary particles in point contact [47]. For the methane nucleation flame ($\varphi = 1.95$), experiments [35] suggest negligible contribution from surface growth and coagulation, so these surface growth and coagulation contributions are excluded from eqs. 2 and 3, consistent with the approach of Kholghy et al. [24]. An equivalent approach was employed by Desgroux et al. [35], who used a low fraction of active sites available for surface reactions to suppress the effect of surface growth. For the sooting methane and the ethylene flames, the D_s employed in the present soot PD model (Supplementary Information, Fig. S2: line) is obtained by fitting the D_s (Supplementary Information, Fig. S2: squares) [18] against the soot volume-equivalent diameter, d_v, derived by DEM at these specific flame conditions [38]:

$$D_s = 2.411 - 0.888\ exp\left(-d_v/8.665\right) \tag{5}$$

The choice of D_s has a negligible effect on f_v predictions at sooting flame conditions (Fig. S3).

The detailed nucleation, surface growth, and coagulation rates employed in eqs. 2 and 3 are discussed in Sections 2.4.1–2.4.3.

2.4.1. Nucleation rate

The soot nucleation rate is traditionally modeled by chemical kinetic models that include detailed reaction mechanisms involved in soot formation. Only a few nucleation rates are determined solely based on the initial fuel concentration and can be directly implemented in eq. 2, bypassing the need for reaction rates of individual reactions. The Moss-Brookes correlation is such a semi-empirical nucleation rate that relies on the C_2H_2 molar concentration, $[C_2H_2]$ [30]:

$$\left(\frac{dN}{dt}\right)^{Nucl.} = C_\alpha N_{Av}\ exp\left(-\frac{T_\alpha}{T}\right)[C_2H_2] \tag{6}$$

where $C_\alpha = 54$ 1/s is a model constant, N_{Av} is the Avogadro number, $T_\alpha = 21{,}100$ K is the activation temperature for nucleation, and T is the reaction temperature. The local $[C_2H_2]$ and T are derived by CHEMKIN PRO as a function of residence time (Supplementary Information: Section S2).

The contribution of nucleation to the rate of change of the total carbon molar concentration in eq. 3 is given by:

$$\left(\frac{dC}{dt}\right)^{Nucl.} = \frac{\rho_{soot}}{MW_c}\frac{\pi d_{\text{crit}}^3}{6}\left(\frac{dN}{dt}\right)^{Nucl.} \tag{7}$$

where $\rho_{soot} = 1500$ kg/m^3 [38] is the nascent soot density, MW_c is the carbon molecular weight, and d_{crit} is the soot critical cluster size. Typically, a pyrene dimer is considered as a representative critical nucleus of soot, corresponding to 32 carbon atoms. Here, the volume-equivalent diameter of a sphere with 36 carbon atoms is used, i.e. $d_{\text{crit}} = 0.97$ nm, corresponding to the critical cluster size obtained by MD (discussed in Fig. 2).

2.4.2. Coagulation

The rate of decrease of the soot agglomerate number concentration due to coagulation is [48]:

$$\left(\frac{dN}{dt}\right)^{Coag.} = -\frac{1}{2}\beta N^2 \rho_{gas} \tag{8}$$

The collision frequency function, β, in the free molecular regime (Knudsen number, $Kn > 10$) is estimated by [49]:

$$\beta = \gamma_{poly}\gamma_{vdW}\ 4\sqrt{\frac{\pi k_B T}{m_{Ag}}}\ d_c^2 \tag{9}$$

where $\gamma_{poly} = 1.35$ [17] is an enhancement factor accounting for primary particle polydispersity during coagulation in the free molecular regime, $\gamma_{vdW} = 2.2$ [50] is the van der Waals enhancement factor for coagulation of small soot particles, k_B is the Boltzmann constant, and d_c and m_{Ag} are the soot agglomerate collision diameter and mass, respectively. All conditions in the present work correspond to $Kn > 60$. The soot mass is determined by:

$$m_{Ag} = \rho_{soot} n_p \pi \frac{d_p^3}{6} \tag{10}$$

where d_p is the primary particle diameter $\left(d_p = \frac{6V}{A}\right)$, and n_p is the number of primary particles per agglomerate $\left(n_p = \frac{6V}{N\pi d_p^3}\right)$ [46]. The collision diameter, d_c, in eq. 9 is calculated by [16]:

$$d_c = \begin{cases} d_p\sqrt{3/5}\,n_p^{\,0.45}, n_p \le 1.8 \\ d_p\dfrac{n_p^{\,0.45}}{n_p^{-0.2}+0.4}, n_p > 1.8 \end{cases} \tag{11}$$

2.4.3. Surface growth

The carbon addition rate due to surface growth in eq. 3 is determined by the hydrogen abstraction-carbon addition mechanism [51]:

$$\left(\frac{dC}{dt}\right)^{SG} = 2k_s\chi_{soot}[C_2H_2]\ \frac{A}{N_{Av}} \tag{12}$$

where k_s is the surface reaction rate coefficient ($k_s = 80\ T^{1.56} exp\left(\frac{-1912.4}{T}\right)$ [51]), χ_{soot} is the number of active sites on the soot particle surface [22]:

$$\chi_{soot} = \alpha\ \chi_{soot-H} \frac{k_f}{k_b} \frac{[H]}{[H_2]} \tag{13}$$

where α is the fraction of available sites ([52]: eq. 43), $\chi_{soot-H} = 2.3 \times 10^{19}$ sites/m^2 [53] is the total number of available surface sites, and k_f and k_b are the forward and backward reaction rates of soot with H in the reaction: $Soot - H + H \underset{\leftarrow k_b}{\overset{\rightarrow k_f}{\rightleftharpoons}} Soot\bullet + H_2$. The $\frac{k_f}{k_b}$ ratio ranges from 0.017 for single aromatic molecules [54] to 1.354 for graphene [55]. Here, an average $\frac{k_f}{k_b} = 0.685$ is used (with sensitivity analysis of this ratio provided in Fig. S4). The time-variant concentrations of atomic, $[H]$, and molecular hydrogen, $[H_2]$, along with $[C_2H_2]$ and T are obtained by CHEMKIN PRO.

3. Results and discussion

3.1. Soot nucleation by MD

Fig. 1 shows 2D snapshots of hydrocarbon molecules and clusters formed during acetylene pyrolysis at 1600 K and residence times, t, of (a) 0.25, (b) 0.5, (c) 0.75, (d) 1, (e) 1.25, and (f) 2 ns. Early on ($t = 0.25$ ns), C_2 dimerization reactions lead to the formation of small linear molecules (Fig. 1a: red molecules), which grow into longer linear molecules upon polymerization (Fig. 1b: red molecules and Fig. S5). During these early stages of acetylene pyrolysis, a wide variety of reactive species and PAH-like molecules are formed [56]. Clusters composed of more than 36 carbon atoms, representing the critical cluster size (as discussed in Fig. 2), first emerge at 0.75 ns (Fig. 1c: purple molecules). As nucleation proceeds (t = 1 ns), the number of critical nuclei and

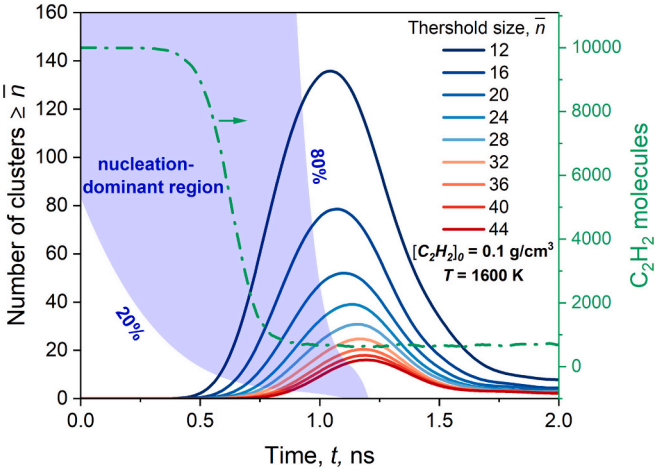

Fig. 2. Temporal evolution of the number of clusters consisting of at least $\bar{n}$ carbon atoms formed during acetylene pyrolysis at T = 1600 K with initial concentration, $[C_2H_2]_0 = 0.1$ g/cm^3. Once the number of C_2H_2 molecules (green dot-broken line, right axis) starts to decrease, the number of clusters with $\bar{n} \geq 12$ increases due to C_2 dimerization and polymerization reactions. The number of clusters for larger $\bar{n}$ (>30) increases later due to nucleation, at around 0.75 ns, before it drops due to cluster-cluster collisions. The nucleation-dominant region for each threshold size (shaded area) is defined as the time during which the number of clusters $\bar{n}$ lies between 20 % and 80 % of the maximum $\bar{n}$. (For interpretation of the references to colour in this figure legend, the reader is referred to the web version of this article.)

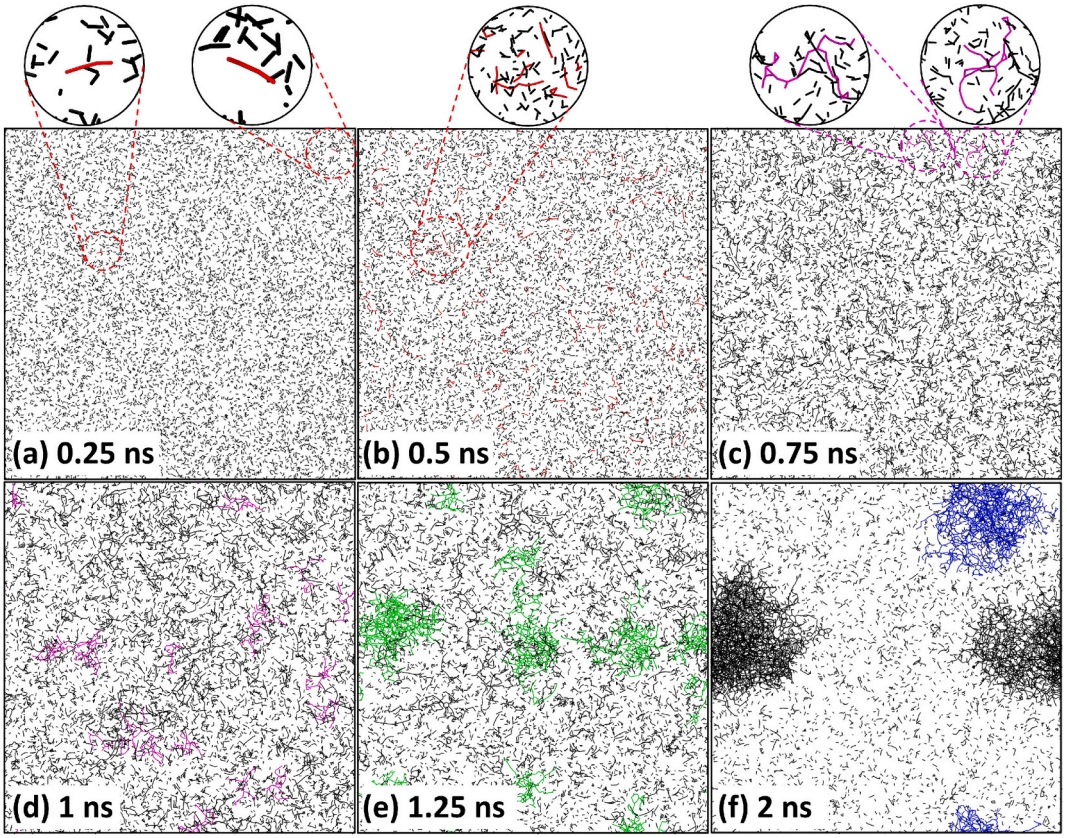

Fig. 1. Snapshots of hydrocarbon molecules and soot clusters formed during acetylene pyrolysis by reactive MD simulations at 1600 K and residence times, t, of (a) 0.25, (b) 0.5, (c) 0.75, (d) 1, (e) 1.25, and (f) 2 ns.

stable clusters increases (Fig. 1d: purple molecules), growing rapidly into larger clusters upon condensation and surface growth at 1.25 ns (Fig. 1e: green molecules) followed by coalescence and further surface growth until the formation of incipient soot nanoparticles (Fig. 1f: black and blue nanoparticles).

Fig. 2 shows the temporal evolution of the number of carbonaceous clusters having at least $\overline{n}$ carbon atoms formed during acetylene pyrolysis at $T = 1600$ K with initial concentration $[C_2H_2]_0 = 0.1$ g/cm^3. The evolution of the cluster count is shown for threshold sizes of $\overline{n} = 12$ (dark blue line) up to 44 (dark red line), along with the temporal evolution of C_2H_2 molecules (green dot-broken line, right axis). For $t \lesssim 0.5$ ns, all molecules have less than 12 carbon atoms as hardly any C_2H_2 molecules have reacted. At $t = 0.5$–1 ns, more than 90 % of the C_2H_2 molecules are rapidly consumed followed by C_2 dimerization and polymerization reactions [57] (Supplementary Information: Fig. S5), and the number of clusters with $\overline{n} \geq 12$ increases almost linearly. Increasing the threshold size, indicating the formation of larger carbonaceous clusters, results in slower nucleation of fewer such species. For example, fewer clusters with $\overline{n} \geq 32$ (light orange line) begin to form at $t \approx 0.75$ ns (Fig. 1c). The number of these large clusters is approximately one order of magnitude lower than that of clusters with $\overline{n} \geq 12$. The concentration of species with $\overline{n} \geq 32$ increases upon nucleation reaching a maximum of 25 at 1.2 ns, followed by a decrease at $t \gtrsim 1.2$ ns as these clusters either react with each other or are scavenged by larger ones, while the C_2H_2 concentration has practically plateaued.

The time where the number of clusters $\overline{n}$ lies between 20 % and 80 % of the maximum cluster concentration for each threshold size denotes a nucleation-dominant region [44], indicated by the shaded area in Fig. 2. Within this region, quasi-steady state nucleation takes place as the number of clusters increases almost linearly with time, with the slope representing the nucleation rate [43]. All clusters with size equal or greater than the critical size are stable, exhibiting a similar formation rate. So, for $\overline{n} \geq 36$ (molecular weight of 432 g/mol), where the slopes of the evolving number of clusters become practically parallel (three consecutive slopes vary less than 15 %), the critical nucleus size has been reached [44]. The critical sizes obtained for different initial C_2H_2 concentrations and process temperatures are shown in Fig. S6, all exhibiting a critical cluster size of ~36 carbon atoms. These results are consistent with size exclusion chromatography and absorption spectra measurements of soot nucleation by pyrene pyrolysis in tubular flow reactors at lower temperatures ($T = 800$–1100 K), indicating a molecular weight of the critical nucleus of at least 400 g/mol [58]. Critical cluster sizes within this range (30–52 carbon atoms) have been proposed by reactive MD simulations for soot formed by *n*-heptane pyrolysis with initial concentration of 0.1 g/cm^3 at high temperature ($T = 2200$–2600 K) using the same approach [33]. The nucleation rate can be obtained by the number of clusters larger than or equal to the critical nucleus size of 36 carbon atoms formed per unit volume per unit time, i.e. the slope of the linearly increasing number of clusters corresponding to the nucleation-dominant region in Fig. 2.

Fig. 3 shows the nucleation rate, J_{MD}, for critical soot clusters, as a function of the initial C_2H_2 molar concentration obtained during isothermal acetylene pyrolysis MD simulations at 1200–1800 K. At low fuel concentration, J_{MD} hardly varies with temperature. Increasing the initial C_2H_2 concentration results in an exponential increase in the nucleation rate with an order dependency of $n = 3.5$ for the employed range of initial acetylene concentrations, regardless of the pyrolysis temperature. A phenomenological model is proposed to describe the dependence of the MD-derived nucleation rate, J_{MD}, on the acetylene concentration for the temperature range employed here:

$$\left(\frac{dN}{dt}\right)^{Nucl.} = J_{MD} = k_{MD}[C_2H_2]^n \tag{14}$$

where k_{MD} is the nucleation rate constant and $n = 3.5$ is the reaction order. Eq. 14 corresponds to a global nucleation rate, where

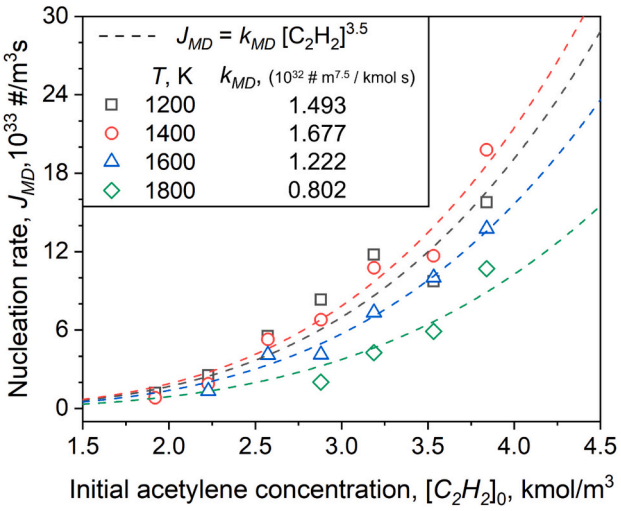

Fig. 3. MD-obtained nucleation rate, J_{MD}, of incipient soot nanoparticles with critical cluster size of 36C atoms as a function of the initial molar concentration for acetylene pyrolysis at $T = 1200$ (squares), 1400 (circles), 1600 (triangles), and 1800 K (diamonds). The nucleation rate is fitted using eq. 14 (lines) to determine the reaction rate constant, k_{MD}.

contributions of intermediate species are accounted for implicitly, resulting in a strong apparent dependence on C_2H_2 concentration. The effect of temperature on the nucleation rate is quantified by k_{MD}, obtained by fitting the fuel concentration-dependent J_{MD} with eq. 14 at each temperature. The k_{MD} shows a minor variation with temperature, ranging between $0.802 \bullet 10^{32}$ to $1.677 \bullet 10^{32}$ $\frac{m^{7.5}}{kmol \bullet s}$. This k_{MD} variation with temperature leads to a PD-predicted difference in soot volume fraction, f_v, of up to 52 % compared to experiments (Fig. S7), which falls within the range of experimental uncertainty reported for both nucleation (±100 %) and sooting flames (±55 %) [35]. Therefore, an average k_{MD} of $1.299 \bullet 10^{32}$ $\frac{m^{7.5}}{kmol \bullet s}$ is used hereafter and the MD-derived nucleation rate becomes:

$$\left(\frac{dN}{dt}\right)^{Nucl.} = J_{MD}\left[\frac{\#}{m^3 s}\right] = 1.299 \bullet 10^{32}\,[C_2H_2]^{3.5} \tag{15}$$

It is noted that eq. 15 has been derived for a temperature range of $T = 1200$–1800 K and the temperature-invariant nucleation rate coefficient may need to be revisited at conditions outside this range, as it may overestimate the soot nucleation rate below 1000 K. Eq. 15 has been derived at high fuel concentrations corresponding to pressures of 189–568 atm and is implemented into the monodisperse PD model (Section 2.4) simulating the dynamics of soot formation in two low-pressure premixed methane flames with equivalence ratios of $\varphi = 1.95$ and 2.32 (Section 3.2).

3.2. Soot particle dynamics in methane premixed flames

Fig. 4 shows the soot volume fraction, f_v, as a function of height above the burner (HAB) in the nucleation flame ($\varphi = 1.95$), predicted by the monodisperse PD model (lines) with the nucleation rate obtained by MD (eq. 15; solid line) and by Moss-Brookes (eq. 6; broken line), excluding contributions from surface growth and coagulation. The PD-predicted f_v is compared with soot volume fraction measurements in the nucleation flame (circles [35]). The f_v increases abruptly with increasing HAB up to 0.5 cm, regardless of the employed nucleation model. This increase in f_v is associated with an increase in the nucleation flame temperature and the concurrent production of acetylene from methane decomposition, promoting the formation of soot nuclei. At HAB > 0.5 cm, f_v increases with a slower rate approaching 160 ppt when the Moss-Brookes nucleation model (broken line) is used, significantly

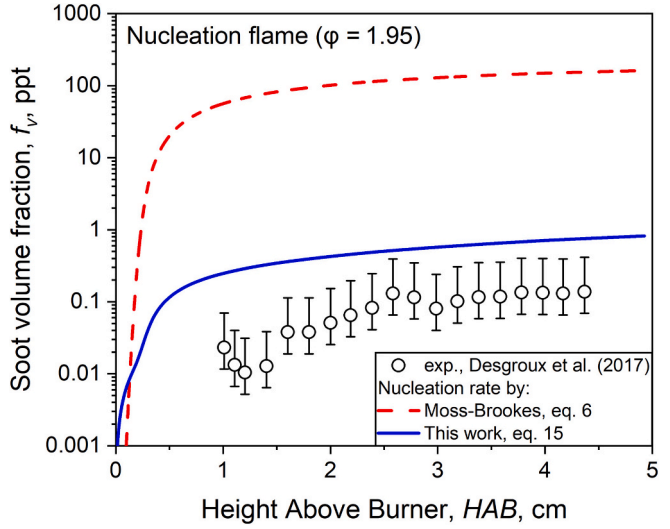

Fig. 4. Soot volume fraction, f_v, as a function of height above the burner (HAB) in nucleation methane flame (φ = 1.95), predicted by the monodisperse PD model (lines) excluding surface growth and coagulation, using the MD-derived (eq. 15; solid line) and Moss–Brookes nucleation model (eq. 6; broken line). The MD-obtained nucleation rate is in agreement (within the same order of magnitude) with soot volume fraction measurements (circles [35]).

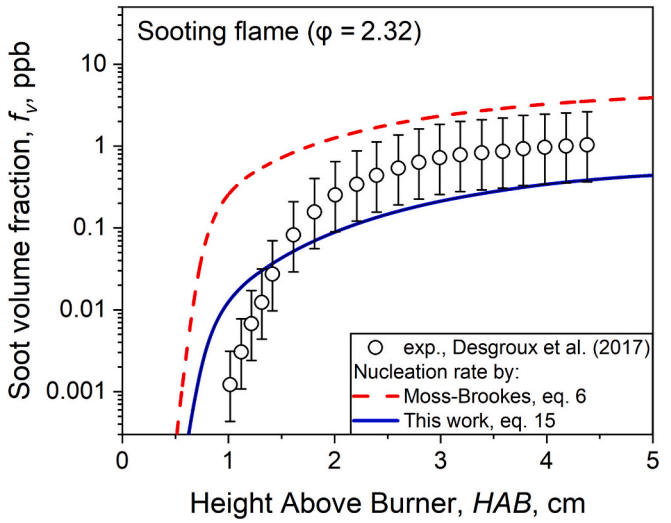

Fig. 5. Soot volume fraction, f_v, as a function of height above the burner (HAB) in sooting methane flame (φ = 2.32), obtained by the monodisperse PD model (lines) accounting for surface growth, coagulation, and nucleation using the MD-derived (eq. 15; solid line) and Moss–Brookes nucleation model (eq. 6; broken line). The f_v is compared with soot volume fraction measurements in the sooting flame (circles [35]).

overpredicting the measured f_v (circles) across the nucleation flame by nearly three orders of magnitude. When the MD nucleation rate (eq. 15) is used, the PD model predicts f_v = 0.8 ppt at HAB = 5 cm, on par with measurements [35] exhibiting f_v = 0.01–0.14 ppt at HAB = 1–4.5 cm, confirming the validity of the proposed nucleation rate for nucleation-dominant soot growth. Even though the MD-proposed nucleation rate has been derived at high fuel concentrations (Section 3.1), soot volume fraction calculations based on this model are in good agreement with experiments (Fig. 4 and Fig. S8), significantly improving predictions from the semi-empirical C_2H_2-based nucleation model [30]. The remaining deviation from experiments is within the measurement uncertainty as laser-induced incandescence only detects particles capable of absorbing light at 1064 nm [59]. However, caution is needed when eq. 15 is applied near atmospheric pressures.

The proposed MD nucleation rate is also applied to sooting flames, where additional soot growth mechanisms, i.e. surface reactions and coagulation, take place. Fig. 5 shows the f_v as a function of HAB in the sooting methane flame with φ = 2.32, as predicted by the monodisperse PD model using the MD-derived (solid line) and Moss-Brookes nucleation rates (broken line) and as obtained by measurements in the sooting flame (circles [35]), with soot primary particle diameter predictions shown in Fig. S9.

At low HAB, the increase in f_v is primarily driven by nucleation, as also observed in the nucleation methane flame (Fig. 4). Once soot nuclei have been formed, they grow through surface reactions, leading to a further increase in the soot volume fraction at higher HAB. The f_v by both nucleation rates increases with HAB. The Moss-Brookes nucleation rate, however, consistently overpredicts the soot volume fraction measurements (circles) by approximately 1 (at high HAB) to 3 orders of magnitude (at low HAB). The MD-derived nucleation rate overpredicts the f_v at HAB <1.5 cm by up to 1 order of magnitude, but underestimates it by up to a factor of 3.4 at higher HAB. This could be partly attributed to the fixed absorption function used to measure f_v [35]. In such premixed flames, the absorption function increases with HAB, so neglecting the size-dependent absorption function of incipient soot may result in underprediction of f_v at small HAB and overprediction further downstream [60]. Even though both nucleation models predict an earlier onset of soot formation than that observed by experiments, the MD-based one follows the measured f_v more closely at low HAB compared to the Moss-Brookes model. The earlier predicted onset of soot formation arises from the fact that, under real flame conditions, acetylene does not directly produce soot nuclei. Instead, it undergoes a series of chemical reactions to form PAHs, which then drive soot nucleation.

The MD-derived nucleation rate is also benchmarked against a burner-stabilized stagnation (BSS) ethylene flame [38] (Supplementary Information: Section S3). Even though the BSS temperature profile (Fig. S10) spans a wider range than the temperature the MD-based rate was developed for, it yields improved soot volume fraction predictions compared to the Moss-Brookes model (Fig. S12b and S15b), demonstrating its potential applicability to other fuels.

4. Conclusions

Soot nucleation is investigated during isothermal acetylene pyrolysis using reactive molecular dynamics (MD) over a flame temperature range of 1200–1800 K. A soot nucleation rate equation is proposed as a function of the initial fuel concentration, by tracking the formation of soot clusters with time in high-pressure MD simulations. The MD-obtained nucleation rate, derived in the temperature range of 1200–1800 K, shows a 3.5-order dependence on the initial acetylene concentration. This rate is validated in premixed flames by employing a monodisperse particle dynamics model accounting for concurrent nucleation, surface growth, and coagulation. The soot volume fraction predicted by the monodisperse model with the nucleation rate obtained by MD is in excellent agreement with measurements in both nucleation (φ = 1.95) and sooting (φ = 2.32) methane premixed flames. So, even though the nucleation rate effectively depends only on C_2H_2 concentration, which may affect the predicted localized soot concentration compared to PAH-based mechanisms, it reliably predicts the overall soot volume fractions. This work demonstrates that MD can provide reliable lumped nucleation rates, which, despite being developed over a narrow temperature range (1200–1800 K), can effectively serve as an alternative to cumbersome chemical kinetic mechanisms in premixed flames. The proposed MD-informed particle dynamics model can be directly integrated into computational fluid dynamics simulations without relying on complex chemical reaction pathways for nucleation. This approach allows for connecting operating conditions with soot yield predictions for the design of cleaner combustion systems.

CRediT authorship contribution statement

A. Fakharnezhad: Writing – original draft, Software, Methodology, Formal analysis, Conceptualization. **G.A. Kelesidis:** Writing – review & editing. **J.D. Berry:** Writing – review & editing. **E. Goudeli:** Writing – review & editing, Supervision, Resources, Project administration, Methodology, Conceptualization.

Declaration of competing interest

None.

Acknowledgements

This work was supported by the University of Melbourne Computing Services and the National Computational Infrastructure (NCI Australia). JDB received support from an Australian Research Council Future Fellowship (FT220100319) funded by the Australian Government.

Appendix A. Supplementary data

DEM-obtained soot surface fractal dimension, details of residence time calculation, BSS ethylene flame soot modeling, and figures showing the workflow of the soot modeling, effect of $\frac{k_f}{k_b}$ ratio and k_{MD}, temporal evolutions of the number of abundant species during acetylene MD pyrolysis, and critical cluster size vs. C_2H_2 concentration and temperature. Supplementary data to this article can be found online at [https://doi.org/10.1016/j.powtec.2025.121747].

Data availability

Data will be made available on request.

References

[1] C.J. Smith, P.M. Forster, M. Allen, J. Fuglestvedt, R.J. Millar, J. Rogelj, K. Zickfeld, Current fossil fuel infrastructure does not yet commit us to 1.5 degrees C warming, Nat. Commun. 10 (2019) 101.
[2] K. Kohse-Hoinghaus, Combustion in the future: the importance of chemistry, Proc. Combust. Inst. 38 (2020) 1–56.
[3] H. Bockhorn, Soot Formation in Combustion: mechanisms and Models, Springer Science & Business Media, 2013.
[4] H.A. Michelsen, Probing soot formation, chemical and physical evolution, and oxidation: a review of in situ diagnostic techniques and needs, Proc. Combust. Inst. 36 (2017) 717–735.
[5] A. Kazakov, M. Frenklach, Dynamic modeling of soot particle coagulation and aggregation: implementation with the method of moments and application to high-pressure laminar premixed flames, Combust. Flame 114 (1998) 484–501.
[6] M.E. Mueller, G. Blanquart, H. Pitsch, A joint volume-surface model of soot aggregation with the method of moments, Proc. Combust. Inst. 32 (2009) 785–792.
[7] C. Saggese, S. Ferrario, J. Camacho, A. Cuoci, A. Frassoldati, E. Ranzi, H. Wang, T. Faravelli, Kinetic modeling of particle size distribution of soot in a premixed burner-stabilized stagnation ethylene flame, Combust. Flame 162 (2015) 3356–3369.
[8] Q. Zhang, H. Guo, F. Liu, G.J. Smallwood, M.J. Thomson, Modeling of soot aggregate formation and size distribution in a laminar ethylene/air coflow diffusion flame with detailed PAH chemistry and an advanced sectional aerosol dynamics model, Proc. Combust. Inst. 32 (2009) 761–768.
[9] N.A. Eaves, Q. Zhang, F. Liu, H. Guo, S.B. Dworkin, M.J. Thomson, CoFlame: a refined and validated numerical algorithm for modeling sooting laminar coflow diffusion flames, Comput. Phys. Commun. 207 (2016) 464–477.
[10] B. Sun, S. Rigopoulos, A. Liu, Modelling of soot coalescence and aggregation with a two-population balance equation model and a conservative finite volume method, Combust. Flame 229 (2021).
[11] A. Liu, S. Rigopoulos, A conservative method for numerical solution of the population balance equation, and application to soot formation, Combust. Flame 205 (2019) 506–521.
[12] M. Balthasar, M. Frenklach, Detailed kinetic modeling of soot aggregate formation in laminar premixed flames, Combust. Flame 140 (2005) 130–145.
[13] G.A. Kelesidis, E. Goudeli, S.E. Pratsinis, Flame synthesis of functional nanostructured materials and devices: surface growth and aggregation, Proc. Combust. Inst. 36 (2017) 29–50.
[14] J. Moran, J. Yon, A. Poux, Monte Carlo Aggregation Code (MCAC) part 1: fundamentals, J. Colloid Interface Sci. 569 (2020) 184–194.
[15] D. Hou, C.S. Lindberg, M.Y. Manuputty, X. You, M. Kraft, Modelling soot formation in a benchmark ethylene stagnation flame with a new detailed population balance model, Combust. Flame 203 (2019) 56–71.
[16] G.A. Kelesidis, E. Goudeli, S.E. Pratsinis, Morphology and mobility diameter of carbonaceous aerosols during agglomeration and surface growth, Carbon 121 (2017) 527–535.
[17] E. Goudeli, M.L. Eggersdorfer, S.E. Pratsinis, Coagulation of agglomerates consisting of polydisperse primary particles, Langmuir 32 (2016) 9276–9285.
[18] M.R. Kholghy, G.A. Kelesidis, Surface growth, coagulation and oxidation of soot by a monodisperse population balance model, Combust. Flame 227 (2021) 456–463.
[19] J.W. Martin, M. Salamanca, M. Kraft, Soot inception: carbonaceous nanoparticle formation in flames, Prog. Energy Combust. Sci. 88 (2022).
[20] Q. Mao, A.C.T. van Duin, K.H. Luo, Formation of incipient soot particles from polycyclic aromatic hydrocarbons: a ReaxFF molecular dynamics study, Carbon 121 (2017) 380–388.
[21] H. Sabbah, L. Biennier, S.J. Klippenstein, I.R. Sims, B.R. Rowe, Exploring the role of PAHs in the formation of soot: pyrene dimerization, J. Phys. Chem. Lett. 1 (2010) 2962–2967.
[22] H. Wang, Formation of nascent soot and other condensed-phase materials in flames, Proc. Combust. Inst. 33 (2011) 41–67.
[23] A. Menon, J.W. Martin, J. Akroyd, M. Kraft, Reactivity of polycyclic aromatic hydrocarbon soot precursors: kinetics and equilibria, J. Phys. Chem. A 124 (2020) 10040–10052.
[24] M.R. Kholghy, G.A. Kelesidis, S.E. Pratsinis, Reactive polycyclic aromatic hydrocarbon dimerization drives soot nucleation, Phys. Chem. Chem. Phys. 20 (2018) 10926–10938.
[25] M.R. Kholghy, N.A. Eaves, A. Veshkini, M.J. Thomson, The role of reactive PAH dimerization in reducing soot nucleation reversibility, Proc. Combust. Inst. 37 (2019) 1003–1011.
[26] F. Schulz, M. Commodo, K. Kaiser, G. De Falco, P. Minutolo, G. Meyer, A. D'Anna, L. Gross, Insights into incipient soot formation by atomic force microscopy, Proc. Combust. Inst. 37 (2019) 885–892.
[27] M. Frenklach, H. Wang, Detailed Mechanism and Modeling of Soot Particle Formation, Soot Formation in Combustion, Springer, 1994, pp. 165–192.
[28] G. Blanquart, P. Pepiot-Desjardins, H. Pitsch, Chemical mechanism for high temperature combustion of engine relevant fuels with emphasis on soot precursors, Combust. Flame 156 (2009) 588–607.
[29] K.M. Leung, R.P. Lindstedt, W.P. Jones, A simplified reaction-mechanism for soot formation in nonpremixed flames, Combust. Flame 87 (1991) 289–305.
[30] S.J. Brookes, J.B. Moss, Predictions of soot and thermal radiation properties in confined turbulent jet diffusion flames, Combust. Flame 116 (1999) 486–503.
[31] G.W. Smith, A simple nucleation/depletion model for the spherule size of particulate carbon, Combust. Flame 48 (1982) 265–272.
[32] F. Schmalz, W.A. Kopp, E. Goudeli, K. Leonhard, Reaction path identification and validation from molecular dynamics simulations of hydrocarbon pyrolysis, Int. J. Chem. Kinet. 56 (2024) 501–512.
[33] A. Fakharnezhad, D.M. Saad, G.A. Kelesidis, E. Goudeli, Nucleation rate of carbonaceous nanoparticles by n-heptane pyrolysis at high pressure and temperature via molecular dynamics simulations, Aerosol Sci. Technol. 59 (2025) 1137–1150.
[34] R.J. Kee, F.M. Rupley, J.A. Miller, Chemkin-II: A Fortran chemical kinetics package for the analysis of gas-phase chemical kinetics, Sandia National Lab.(SNL-CA), Livermore, CA (United States), 1989.
[35] P. Desgroux, A. Faccinetto, X. Mercier, T. Mouton, D.A. Karkar, A. El Bakali, Comparative study of the soot formation process in a "nucleation" and a "sooting" low pressure premixed methane flame, Combust. Flame 184 (2017) 153–166.
[36] A.E. Bakali, X. Mercier, M. Wartel, F. Acevedo, I. Burns, L. Gasnot, J.-F. Pauwels, P. Desgroux, Modeling of PAHs in low pressure sooting premixed methane flame, Energy 43 (2012) 73–84.
[37] A.D. Abid, J. Camacho, D.A. Sheen, H. Wang, Quantitative measurement of soot particle size distribution in premixed flames – the burner-stabilized stagnation flame approach, Combust. Flame 156 (2009) 1862–1870.
[38] J. Camacho, C. Liu, C. Gu, H. Lin, Z. Huang, Q. Tang, X. You, C. Saggese, Y. Li, H. Jung, L. Deng, I. Wlokas, H. Wang, Mobility size and mass of nascent soot particles in a benchmark premixed ethylene flame, Combust. Flame 162 (2015) 3810–3822.

[39] S. Sarl, MAPS Platform, Version 4.4.0, (17 Square Edouard VII 75009 Paris, France, Scienomics, France), 2020.
[40] K. Chenoweth, A.C.T. van Duin, W.A. Goddard, ReaxFF reactive force field for molecular dynamics simulations of hydrocarbon oxidation, Chem. Eur. J. 112 (2008) 1040–1053.
[41] S. Plimpton, Fast parallel algorithms for short-range molecular-dynamics, J. Comput. Phys. 117 (1995) 1–19.
[42] A. Sharma, K.M. Mukut, S.P. Roy, E. Goudeli, The coalescence of incipient soot clusters, Carbon 180 (2021) 215–225.
[43] K. Yasuoka, M. Matsumoto, Molecular dynamics of homogeneous nucleation in the vapor phase. I. Lennard-Jones fluid, J. Chem. Phys. 109 (1998) 8451–8462.
[44] R. Halonen, V. Tikkanen, B. Reischl, K.K. Dingilian, B.E. Wyslouzil, H. Vehkamaki, Homogeneous nucleation of carbon dioxide in supersonic nozzles II: molecular dynamics simulations and properties of nucleating clusters, Phys. Chem. Chem. Phys. 23 (2021) 4517–4529.
[45] Y. Sun, Y. Zhang, M. Huang, Q. Li, W. Wang, D. Zhao, S. Cheng, H. Deng, J. Du, Y. Song, H. Li, H. Xu, Effect of hydrogen addition on the combustion and emission characteristics of methane under gas turbine relevant operating condition, Fuel 324 (2022).
[46] F.E. Kruis, K.A. Kusters, S.E. Pratsinis, B. Scarlett, A simple model for the evolution of the characteristics of aggregate particles undergoing coagulation and sintering, Aerosol Sci. Technol. 19 (1993) 514–526.
[47] Y. Xiong, S.E. Pratsinis, Formation of agglomerate particles by coagulation and sintering—part I. A two-dimensional solution of the population balance equation, J. Aerosol Sci. 24 (1993) 283–300.
[48] S. Friedlander, Smoke, Dust and Haze, Oxford University Press, 2000.
[49] E. Otto, F. Stratmann, H. Fissan, S. Vemury, S.E. Pratsinis, Quasi-self-preserving log-normal size distributions in the transition regime, Part. Part. Syst. Charact. 11 (1994) 359–366.
[50] S.J. Harris, I.M. Kennedy, The coagulation of soot particles with van der Waals forces, Combust. Sci. Technol. 59 (1988) 443–454.
[51] J. Appel, H. Bockhorn, M. Frenklach, Kinetic modeling of soot formation with detailed chemistry and physics: laminar premixed flames of C2 hydrocarbons, Combust. Flame 121 (2000) 122–136.
[52] A. Bouaniche, J. Yon, P. Domingo, L. Vervisch, Analysis of the soot particle size distribution in a laminar premixed flame: a hybrid stochastic/fixed-sectional approach, Flow Turbulence Combust. 104 (2020) 753–775.
[53] M. Frenklach, H. Wang, Detailed modeling of soot particle nucleation and growth, Symp. Combust. 23 (1991) 1559–1566.
[54] H. Wang, M. Frenklach, A detailed kinetic modeling study of aromatics formation in laminar premixed acetylene and ethylene flames, Combust. Flame 110 (1997) 173–221.
[55] R. Whitesides, D. Domin, R. Salomón-Ferrer, W.A. Lester, M. Frenklach, Embedded-ring migration on graphene zigzag edge, Proc. Combust. Inst. 32 (2009) 577–583.
[56] A. Ganguly, K.M. Mukut, S. Roy, G. Kelesidis, E. Goudeli, Investigation of soot precursor molecules during inception by acetylene pyrolysis using reactive molecular dynamics, Aerosol Res. 3 (2025) 185–203.
[57] M. Altarawneh, L. Ali, Formation of polycyclic aromatic hydrocarbons (PAHs) in thermal systems: a comprehensive mechanistic review, Energy Fuel 38 (2024) 21735–21792.
[58] M. Sirignano, C. Russo, Pyrene dimerization in controlled temperature environment: an experimental study, Proc. Combust. Inst. 38 (2021) 1173–1180.
[59] P. Desgroux, X. Mercier, K.A. Thomson, Study of the formation of soot and its precursors in flames using optical diagnostics, Proc. Combust. Inst. 34 (2013) 1713–1738.
[60] G.A. Kelesidis, S.E. Pratsinis, Soot light absorption and refractive index during agglomeration and surface growth, Proc. Combust. Inst. 37 (2019) 1177–1184.